Clement MA, Kilsby CG, Moore P.
[Multi-temporal synthetic aperture radar flood mapping using change detection](https://doi.org/10.1111/jfr3.12303).
Journal of Flood Risk Management
2017
DOI link: https://doi.org/10.1111/jfr3.12303

Copyright:

DOI link to article:

Date deposited:

26/05/2017

Multi-temporal synthetic aperture radar flood mapping using change detection

M.A. Clement[1] [ID], C.G. Kilsby[1,2] and P. Moore[1]

1 School of Civil Engineering and Geosciences, Newcastle University, Newcastle upon Tyne, UK
2 Willis Research Network, London, UK

Abstract

A change detection and thresholding methodology has been adapted from previous studies to determine the extent of flooding for 13 Sentinel-1 synthetic aperture radar images captured during the floods of winter 2015–2016 in Yorkshire, UK. Both available polarisations, VH and VV, have been processed to allow for a comparison of their respective accuracy for delineating surface water. Peak flood extents are found on 29 December 2015 during the aftermath of storms Eva and Frank. Results have been validated against a Sentinel-2 optical image, with both polarisations producing a total accuracy of 97%. Of the two polarisations, VV produces fewer misclassifications, mirroring the similar results reported in previous research. Mapped results are compared to the Environment Agency Flood Maps for Planning (EA FMP), with good correlation observed for inundation on the floodplains. Differences occur away from the floodplains, with the satellite data identifying pluvial flooding not highlighted by the EA FMP.

Introduction

Satellite imagery can determine the extent of flooding over large geographical areas, providing an advantage over *in situ* data sources where the information can have limited spatial and temporal resolution whilst being costly to acquire. In recent years the quantity and quality of satellite products available to stakeholders during and after an event has greatly improved. The Sentinel series of satellites is a prime example of this, producing data with high spatial and temporal resolutions that is free to download. These advances in satellite data sets have led to the development of near real-time, automated flood mapping algorithms (Matgen *et al.*, 2011; Martinis *et al.*, 2015; Twele *et al.*, 2016). As well as providing vital information during an emergency, information derived from satellite imagery can be used to calibrate and validate hydrodynamic models, improving the predictive accuracy, and subsequently increasing stakeholder's understanding of flood dynamics (Schumann *et al.*, 2009; Grimaldi *et al.*, 2016).

Two types of satellite imagery are available at spatial resolutions suitable for monitoring surface water dynamics: optical and synthetic aperture radar (SAR). However, the acquisition and image properties vary, providing challenges when used to monitor hydrology. Optical sensors, such as those onboard the Landsat-8 and Sentinel-2 satellites,

collect data across a variety of spectral bands ranging from the visible spectrum through to shortwave infrared (SWIR). Different land covers display specific reflective characteristics for each spectral band, which can be used to identify areas of water (Xu, 2006; Feyisa *et al.*, 2014). Optical sensors are passive, with the images capturing the solar reflectance of the earth's surface or atmosphere, resulting in the sensor being unable to penetrate cloud cover (Gan *et al.*, 2012). This is the main disadvantage of optical satellites, with flood events potentially occurring without any images being captured, making these sensors a poor choice for monitoring.

SAR systems, such as those on-board the Sentinel-1 satellites, are active sensors which emit a radar pulse and record the land surface return at the satellite. They provide an advantage over optical sensors by enabling collection of data through cloud cover and during the night (Alsdorf *et al.*, 2007; Schlaffer *et al.*, 2015). The strength of the radar return is dependent on a number of factors, notably surface roughness, dielectric properties, and local topography in relation to the radar look angle (Brivio *et al.*, 2002; Gan *et al.*, 2012). Water bodies are a specular reflector of the radar pulse, resulting in minimal signal returned to the satellite (Jung *et al.*, 2010; Schlaffer *et al.*, 2015). Various methods have been used within the literature to delineate water from SAR data, either as a singular process or in

combination. These include histogram thresholding (Brivio *et al.*, 2002; Henry *et al.*, 2006; Brown *et al.*, 2016), fuzzy classification (Martinis *et al.*, 2015; Twele *et al.*, 2016), region growing (Matgen *et al.*, 2011; Mason *et al.*, 2012; Martinis *et al.*, 2015; Twele *et al.*, 2016), and texture analysis (Pradhan *et al.*, 2014). Unlike the above processes, which use a single SAR image, change detection highlights the temporal changes in land cover by comparing the flood scene to a previous dry image (Giustarini *et al.*, 2013; Schlaffer *et al.*, 2015). The difference between the images can be combined with other image segmentation techniques to identify areas producing an unusually low backscatter response, improving the reliability of the flood delineation when compared to the single image methodologies (Matgen *et al.*, 2011).

Despite the operational advantages of SAR compared to optical systems, there are challenges in identifying flooding. Roughening of the water surface, created by heavy rainfall or wind, can cause backscattering of the radar signal, increasing the possibility of inundated areas not being highlighted (Alsdorf *et al.*, 2007; Jung *et al.*, 2010). SAR systems are side looking and, depending on the incidence angle, terrain features can produce radar shadow, overlaying, and foreshadowing (Rees, 2000; Giustarini *et al.*, 2013). In particular, radar shadow can provide difficulties in hydrological studies, creating anomalous dark areas within the radar image which can be misclassified as water. Identification of flooding can also be problematic in areas where other structures protrude the water surface and interact with the radar signal. This causes the double-bounce effect, with the signal reflecting off the water surface before interacting with the vertical structure, creating a corner reflector, and a strong return signal at the satellite (Horritt *et al.*, 2001; Jung *et al.*, 2010; Giustarini *et al.*, 2013). The high density of buildings in urban areas can cause both radar shadow and double-bounce, limiting the delineation of flood extents without the use of expensive ultra-high resolution SAR data, such as TerraSAR-X, RADARSAT-2 or COSMO-SkyMed (Giustarini *et al.*, 2013; Pulvirenti *et al.*, 2016). However, the ability of SAR sensors to penetrate cloud cover, along with the improvements in the spatial and temporal resolution of freely available data sets, demonstrates the key role SAR has in rural flood monitoring and management.

The aim of this research is to move towards near real-time determination of flood extents using multi-temporal satellite SAR data sets, with methods that are both quick and easy to apply over large areas as new data becomes available. The case study of the 2015–2016 UK winter storm season has been selected to test the reliability of the process. The derived flood extent will be validated against cloud free optical data and modelled flood maps. The results will provide an insight into the flood extent change over a 5-week period, providing information on flood dynamics, as well as highlighting pluvial flooding away from the floodplains.

Methodology

Location

A 400 km^2 study area was selected in Yorkshire, UK, for testing of the proposed methodology. The region, shown in Figure 1, stretches from the south of York down to Selby, and west beyond Tadcaster. The area is largely rural, with two major rivers flowing through it: the Wharfe and Ouse. The region suffered from spatially and temporally variable flooding during December 2015 and January 2016, when storms Desmond (5–6 December 2015), Eva (24 December 2015), and Frank (29–30 December 2015) brought widespread rainfall across northern UK.

Data

The 13 Sentinel-1 SAR images collected over the study region between 5 December 2015 and 10 January 2016 are listed in Table 1. Radiometrically calibrated and terrain corrected Sentinel-1 images are stored within Google Earth Engine (GEE), which provides free cloud computing facilities for research, with the change detection processing completed within this infrastructure (GEE, 2015).

Sentinel-1, part of the European Space Agency Copernicus programme, consists of two satellites launched on 3 April 2014 and 22 April 2016. The satellites are in opposite polar sun-synchronous orbits at an altitude of 693 km, with a repeat cycle of 12 days, containing 175 orbits. This results in a repeat frequency of 24 hours at high latitudes and 3 days at the equator. The SAR system operates within C-band (5.407 GHz) frequencies in one of four acquisition modes: Stripmap (SM), Interferometric Wide swath (IW), Extra-Wide swath (EW), and Wave (WV). IW is the default mode over land, operating under the TOPSAR (Terrain Observation with Progressive Scans SAR) principle (Geudtner *et al.*, 2014). During acquisition the radar scans in both the azimuth and range directions simultaneously to provide three sub-swaths with a 2 km overlap (De Zan and Guarnieri, 2006). Each sub-swath contains six bursts, which are processed individually as single look complex (SLC) scenes, before being resampled to 10 × 10 m pixel spacing, deburst and merged into one tile. Data is collected in 250 km swaths at incidence angles between 29.1° and 46.0°, providing a ground resolution of 5 × 20 m (range × azimuth). The user guide (https://sentinel.esa.int/web/sentinel/user-guides/sentinel-1-sar) provides further information on the satellite's acquisition parameters.

The polarisation of SAR images refers to the geometric plane that the radar wavelength is transmitted and received

Figure 1 The 400 km^2 study region, shown by the red box, for which flood extents have been determined for December 2015 and January 2016. Background and location maps throughout article © Crown Copyright/database right 2017. An Ordnance Survey/EDINA supplied service.

along. In most systems these are either horizontal (H) or vertical (V) in relation to the satellite antenna, creating four common polarisations: HH, HV, VH, and VV. Although each polarisation can be used for flood delineation, the backscatter characteristics of the radar signal varies, impacting the accuracy of the inundation maps produced. Manjusree *et al.* (2012) compared the four polarisations, concluding that HH has the greatest

potential for delineating flooding consistently and accurately, results mirrored in other research (Henry *et al.*, 2006; Brisco *et al.*, 2008). Sentinel-1 collects images in VH and VV polarisation when in IW mode, both of which have the potential for classification errors. Cross-polarised data (VH and HV) produces a wider range of backscatter values from vegetated land surfaces compared to co-polarised data (VV and HH), leading to potential overlap

Table 1 List of Sentinel-1 scenes used, the date, the percentage of study area covered, the satellite track ID and the number of images used to calculate the reference image

Sentinel-1 image	Date	Footprint (%)	Track ID	No. of ref. images
S1A_IW_GRDH_1SDV_20151205T061404_20151205T061429_008903_00CBC9_2323	05/12/2015	100	81	18
S1A_IW_GRDH_1SDV_20151208T174942_20151208T175007_008954_00CD3E_349B	08/12/2015	100	132	4
S1A_IW_GRDH_1SDV_20151210T062205_20151210T062230_008976_00CDE1_1951	10/12/2015	100	154	10
S1A_IW_GRDH_1SDV_20151213T175808_20151213T175833_009027_00CF27_4F38	13/12/2015	68.1	30	7
S1A_IW_GRDH_1SDV_20151217T061404_20151217T061433_009078_00D09B_ECA6	17/12/2015	100	81	18
S1A_IW_GRDH_1SDV_20151220T174947_20151220T175012_009129_00D20A_C0F7	20/12/2015	100	132	4
S1A_IW_GRDH_1SDV_20151222T062204_20151222T062229_009151_00D2AF_17F0	22/12/2015	100	154	10
S1A_IW_GRDH_1SDV_20151225T175803_20151225T175828_009202_00D428_9464	25/12/2015	68.2	30	7
S1A_IW_GRDH_1SDV_20151229T061403_20151229T061428_009253_00D59B_CC2A	29/12/2015	100	81	18
S1A_IW_GRDH_1SDV_20160101T174941_20160101T175006_009304_00D70A_60DE	01/01/2016	100	132	4
S1A_IW_GRDH_1SDV_20160103T062204_20160103T062229_009326_00D7AC_C9F2	03/01/2016	100	154	10
S1A_IW_GRDH_1SDV_20160106T175807_20160106T175832_009377_00D920_8394	06/01/2016	68.4	30	7
S1A_IW_GRDH_1SDV_20160110T061404_20160110T061433_009428_00DA93_B5C5	10/01/2016	100	81	18

with the low backscatter values associated with water, causing misclassification of land as flooded (Manjusree *et al.*, 2012; Twele *et al.*, 2016). VV polarised wavelengths are more susceptible to roughening of the water surface, commonly caused by wind or rain, increasing the backscatter return to the satellite, resulting in inundation not being identified (Manjusree *et al.*, 2012). The limitations of each polarisation as environmental conditions vary requires acknowledgement when using Sentinel-1 for flood mapping. Previous research concluded that VV provides a slight advantage when identifying flooding when using Sentinel-1 data (Twele *et al.*, 2016). To allow for further comparison both polarisations have been processed using the same methods within this study.

Within the methodology a terrain filter is applied to remove areas where the topographical location suggests that flooding is unlikely, but where SAR image acquisition may result in misclassification. For this the Ordnance Survey 5 m Digital Terrain Model (DTM) was used to create Height above Nearest Drainage (HAND) and slope data sets. The slope aspect of the filter is required to remove areas of radar shadow, found when large vertical structures limit the ability of the SAR system to record data from the lee of the feature. The minimal radar response in these areas is similar to that of flat water. The HAND data set represents the topographic difference between a pixel and its hydrologically determined nearest water course (Rennó *et al.*, 2008; Nobre *et al.*, 2011). The addition of HAND reduces the impact of the slope filter in the lowlands by including features such as river banks, which would be otherwise removed. For this project a HAND threshold of 20 m, along with 3° slope, were combined to create the terrain filter.

A cloud free satellite optical image was collected by Sentinel-2 on 29 December 2015, 12 hours after the Sentinel-1 pass. The use of optical imagery to validate SAR

water extractions has become common practice, despite the potential errors in classifying water using optical data. However, the lack of *in situ* data to act as a reference means the Sentinel-2 image has been used to validate the SAR flood extents. To extract the water bodies from the optical image the modified normalised difference water index (MNDWI) was applied, defined by Xu (2006) as:

$$MNDWI = \frac{Green - SWIR}{Green + SWIR} \tag{1}$$

with band 3 and band 11 representing the green and SWIR wavelengths within the Sentinel-2 instrumentation. The MNDWI highlights the strong absorption of SWIR radiation by water bodies, improving on other water extraction indices, notably the normalised difference water index (NDWI) (McFeeters, 1996), by providing better separation between water and urban areas. The MNDWI data set can theoretically be segmented at zero to identify areas of water, however, differences in sensor acquisition parameters and geographical image characteristics can create a differing range of values, necessitating the need for individual image thresholding. To achieve this Otsu's method was employed, maximising the variance between the water and land classes (Otsu, 1979). The SAR and MNDWI flood extents have been compared, with the producer's (flooding misclassified as land), user's (land misclassified as flood) and total accuracies calculated, along with Cohen's kappa coefficient (κ – agreement that is not caused by chance).

The Environment Agency Flood Maps for Planning (EA FMP) contain modelled indicative results of areas likely to be inundated during a 100-year river or 200-year sea flood event (known as Zone 3, referred as 100-year event henceforth), as well as a 1000-year event from either source (Zone 2) (Porter and Demeritt, 2012). The extents have been modelled using a DTM with the flood defences

removed, allowing for a subsequent data set highlighting the areas protected by the current flood defences during a 100-year event. A further map showing the areas designated for storage areas is available, with these locations used to attenuate the flood peak in vulnerable areas. The SAR-derived flood extents have been compared to the EA FMP, providing a comparison between the remote sensing data and modelled results. Within the study region, a 100-year flood would inundate 53.4 km^2 of the area (13.4% of the study region), including 10.4 km^2 classed as water storage areas (2.6%), with an additional 24.9 km^2 being actively protected by defences (6.2%).

An aerial photograph, taken on 27 December 2015 by the National Police Air Service (NPAS) Carr Gate helicopter, has been used to provide supplementary information about the hydrological conditions in the region prior to the satellite crossing. The image was taken as the helicopter was to the west of the study region, close to Tadcaster on the river Wharfe. The image looks eastwards, towards the confluence of the Ouse and the Wharfe.

Processing steps

A change detection and thresholding (CDAT) methodology, adapted from Long *et al.* (2014), was used to determine the flooding extent. Figure 2 provides a diagrammatic overview of the workflow. The first step requires a non-flood reference image for change detection. Selection of this image can influence the outcome, with seasonal differences in land use and variances in satellite acquisition parameters (e.g. orbit direction and incidence angle) requiring consideration (Hostache *et al.*, 2012). The reference images in this study were calculated using a collection of 39 previous Sentinel-1 images, dated between 3 July 2015 and 5 November 2015. Ideally the time period used to create the reference collection would be similar to that of the flooding. However, due to the relatively short time Sentinel-1 has been operational, the majority of winter images suffer from either flooding or poor pre-processing within GEE, leading to the inclusion of summer images to ensure coverage for each satellite track. For each flood scene analysed, the images with the same
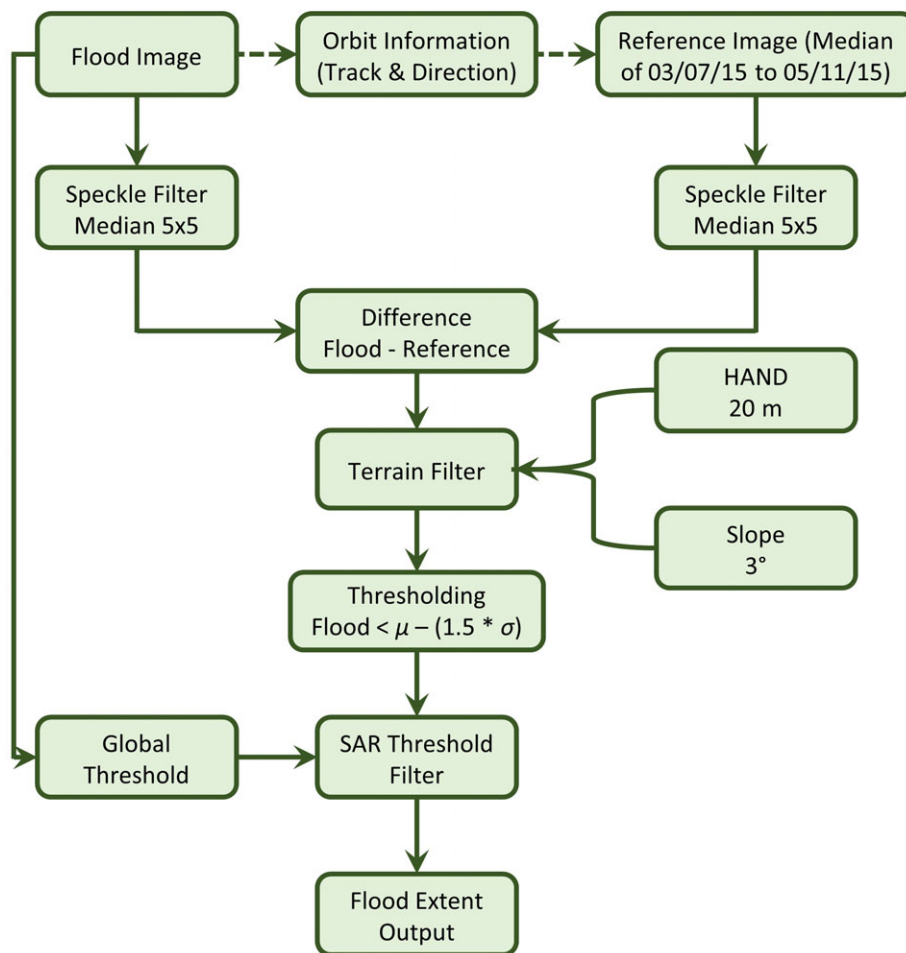

Figure 2 Workflow used to extract the flooding extents for this study. μ and σ represent the mean and standard deviation.

satellite track are selected, with the median value from this subset taken for each pixel to create the final reference image. Four different satellite tracks provide coverage over the study area, with the number of images in each reference image collection ranging from 4 to 18, as summarised in Table 1.

SAR suffers from speckle due to the variation in the radar return within a pixel caused by multiple scattering sources, such as vegetation (Esch *et al.*, 2011; Giustarini *et al.*, 2015). Filters can be applied to remove speckle, leaving a smoother image that can be used more accurately in further processing. Both the flood and reference images had a median 5×5 pixel filter applied for this purpose. The difference between the flood and reference image is calculated under the premise that change detection highlights variations in the radar return to the satellite, and by proxy changes in land cover or conditions. It is expected that flooding will cause a large negative difference due to the specular reflection of the radar signal by water, compared to the normal, stronger land backscatter response.

The difference image is subsequently filtered based on terrain, with composition and parameters of the filter described previously. The application of the filter removes just over 8 km^2, or 2%, of the region. A threshold approach is applied to the difference image to extract the largest negative change in backscatter, thus highlighting areas most likely to be inundated. Long *et al.* (2014) determined the ideal threshold to be:

$$P_F < (\{\mu[D] - f_c * \{\sigma[D]\}) \tag{2}$$

where P_F are the pixels identified as flooded, μ and σ the mean and standard deviation of D, the difference image, and f_c is a coefficient. Optimal f_c was found to be 1.5 by Long *et al.*

A second filter was applied to the extracted inundation extent based on the flooded SAR image, an additional step compared to the original CDAT methodology. This is due to seasonal changes in land cover occasionally producing similar decreases in backscatter as flooding within the difference image. For this filter, a global threshold for the land-water boundary was defined based on the histograms of the SAR images used in the study, with only the areas identified as flooding by both the SAR threshold and the CDAT process used as the final flood extent.

The results are mapped, allowing direct comparisons between the two polarisations, as well as the Sentinel-2 optical data set and the EA FMP. An estimate is also made of the number of days each pixel was inundated during the 37-day study period. Each satellite image has been allocated a number of days, calculated as an even distribution of the time between the preceding and following satellite passes. For each pixel, the image scores for the dates when flooding has been identified are summed to provide an estimate for the number of days the pixel was inundated. The study area has been sub-divided for this purpose, with different weightings required when the images do not cover the full region.
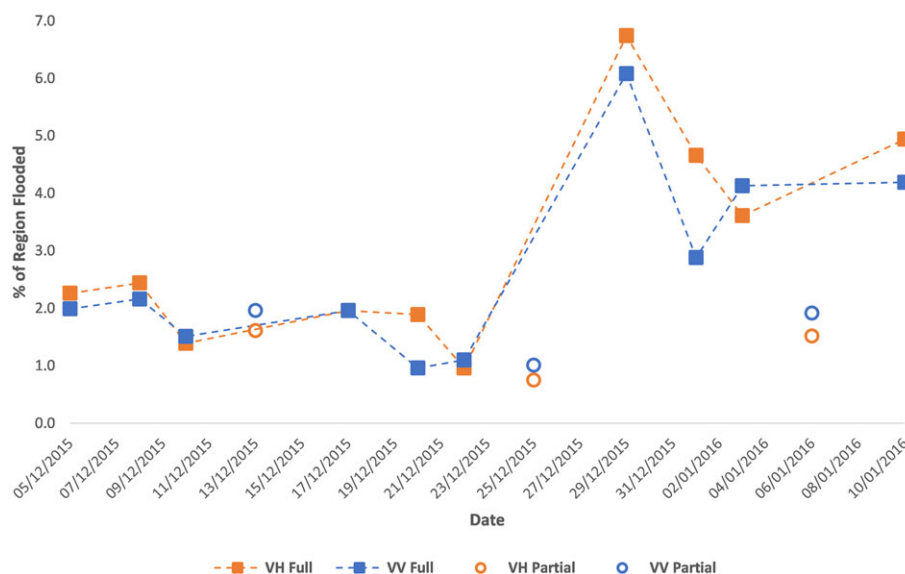

Figure 3 Percentage of region identified as flooded for the VH and VV polarisations. Dates with full satellite coverage are joined to show the approximate sequence of flooding. Other data points, labelled as partial, have 68% of the region covered by Sentinel-1 and are likely to underestimate the extent of flooding.

Results

Polarisation comparison

Both polarisations display a similar sequence for the amount of flooding throughout the study period (Figure 3). The image collected on 29 December provides the maximum flood extent for both polarisations, showing the aftermath of storms Eva and Frank. On this date, 6.7% and 6.1% of the study region were inundated for VH and VV, respectively. Preceding this date is a slight downwards trend in flood extent from the initial image on 5 December, with extents of 2.3% (VH) and 2.0% (VV), to 25 December, with 0.7% (VH) and 1.0% (VV) of the region inundated. A decrease in flood extent is observed following 29 December, before an increase on 10 January to 4.9% (VH) and 4.2% (VV), the second greatest extent observed.

Both VH and VV polarisations are available for all images, allowing a comparison of their ability to delineate flooding. The observed time-series between the two data sets are similar, as seen in Figure 3. The satellite crossing on 17 December provides a match in the extent of flooding between the two polarisations, although only 80.4% of the identified areas correspond. All other images provide differing flooding extents between VH and VV, with an even split for the greatest estimator. Figure 4 shows the relationship between the two data sets. A strong linear distribution is observed, with an R^2 value of 0.87. At lower extents of flooding VV identifies a greater area of inundation, with the polarisations matching at 1.6%. As the extent of
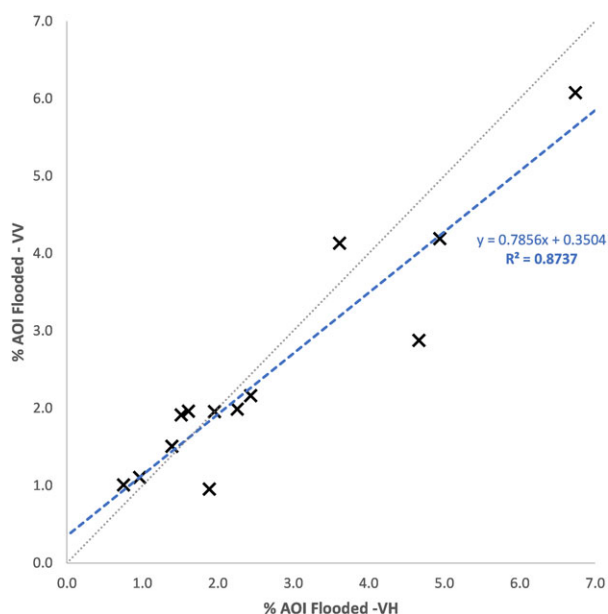
flooding grows, VH identifies an increasingly greater proportion of the region as inundated compared to VV, with 6.0% in VH equating to 5.1% in VV.

Two dates show a considerable difference between the two polarisations. On 20 December, the flood extent from VH (1.9%) is almost double that of VV (1.0%), with the VH identifying potential pluvial flooding that is missed by the VV. Similarly on 1 January, VV (2.9%) identifies just 61.7% of the flood extent as estimated from VH (4.7%). On this date, the difference is largely within the main body of flooding, with the VH identifying a uniform water surface compared to the smaller separate areas seen in the VV (Figure 5). It can be hypothesised that the lack of consistency in the VV backscatter response is caused by the wind roughening of the water surface.

Validation

The MNDWI water extent of the Sentinel-2 optical image of 29 December has been used to validate the flood extents from the two polarisations of the SAR image collected on the same day. The accuracies of both polarisations are shown in Table 2. Producer's accuracy for identifying flooded pixels is slightly better with VH, showing a greater inclusion of Sentinel-2 identified water pixels in the flood extent. However, VV produces 94.3% user's accuracy compared to 87.0% for VH, showing less misclassification of land as water using this polarisation. Overall the total accuracies are similar with 0.4% difference. The kappa coefficient (κ) varies from 0.778 for VH to 0.799 for VV, showing a good relationship between the optical result and the two polarisations, with minimal correlation caused by chance.

Figure 6 provides a mapped comparison between flood extents from the SAR and optical data sets. There is good correlation between the three data sets for the large area of water which represents the inundated floodplain next to the Wharfe and Ouse rivers. The differences between the data sets can be characterised in four ways: permanent water bodies identified in the optical image but not in the SAR, misclassification of shadow areas as water within the optical image, extraction of the edges of flat man-made features within the SAR, and potential misclassification of land within the VH SAR image.

Both VH and VV polarisations have identified the edges of some urban features as flooded. This is most notable with the flat tarmac associated with an airport, highlighted in Figure 6, which provides a similar specular reflectance as water. There are matching flood extents between the Sentinel-2 validation data set and the VV polarisation in these areas on 29 December. The VH polarisation identifies additional sections of the runway edges as inundated compared to the other imagery. The suggested flooding may be
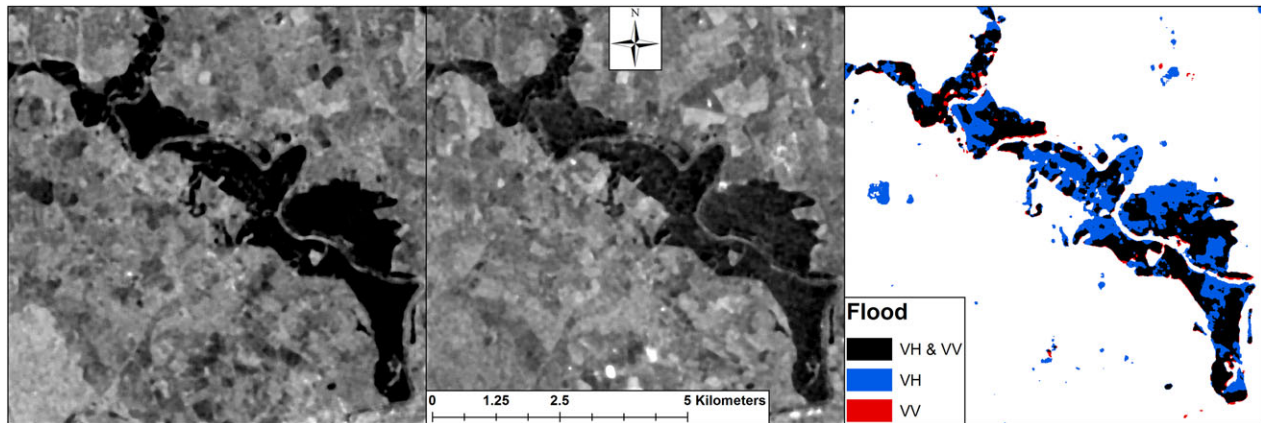

Figure 4 Relationship between the percentages of the study region identified as flooded for the VH and VV polarisations. Grey line represents $y = x$ as reference.

Figure 5 Comparison of the flood extents from 1 January 2016. (Left) VH SAR image. (Middle) VV SAR image. (Right) Derived flood extents. Note VV shows an inconsistent body of water compared to VH due to increased backscatter on the water surface in the SAR image, likely caused by wind roughening of the water.

correct, however, caution is required due to the potential for misclassification around these features.

Areas of pluvial flooding are highlighted in locations away from the floodplains. These areas, likely to be agricultural fields that have become partially inundated, are more readily identified with the VH polarisation. Both polarisations identify smaller fields not classed as water in the MNDWI, with VH also extracting some larger areas. The VV flood extents provide a better match to the MNDWI data set, suggesting the additional flood areas identified with the VH are unlikely to be accurate. However, the misclassification of shadows as water within the reference data set can complicate the accuracy assessment of the SAR-derived flood maps when using optical data as a reference.

Table 2 Error matrices showing the accuracy of the methodology for both polarisations. The MNDWI computed from a Sentinel-2 scene acted as a reference data set. Italic values represent km² and bold values are percentages. Total accuracy for VH was 97%, with a Cohen's κ of 0.778 (0 = relationship is chance, 1 = perfect relationship). Total accuracy for VV was 97.4%, with a κ of 0.799

VH	Reference Sentinel-2			
SAR – Sentinel-1	No flood	Flood	SAR total	**User's %**
No flood	*364.4*	*8.7*	*373.1*	**97.7**
Flood	*3.5*	*23.4*	*26.9*	**87.0**
Ref. total	*367.9*	*32.1*	*400.0*	
Producer's %	**99.0**	**73.0**		

VV	Reference Sentinel-2			
SAR – Sentinel-1	No flood	Flood	SAR total	**User's %**
No flood	*366.5*	*9.2*	*375.7*	**97.6**
Flood	*1.4*	*22.9*	*24.3*	**94.3**
Ref. total	*367.9*	*32.1*	*400.0*	
Producer's %	**99.6**	**71.5**		

An aerial image from 27 December, captured by the NPAS Carr Gate police helicopter, has been used to provide secondary validation of the results (Figure 7). The image has been geolocated based on road and railway locations, visible above the flood water in both data sets. Although the image is 2 days before the satellite crossing, the similarities are good, with the main flooded regions showing a match. Despite the lack of statistical metrics, there is still benefit in comparing the satellite data with other sources of imagery to confirm the results.

Flood dynamics

The multiple satellite images of the region over the study period enabled tracking of the advance and retreat of the flood waters. A good example is the recession of the peak event on 29 December, through two satellite passes on 1 January and 3 January (Figure 8). At first inspection, the polarisations show a similar pattern of recession, particularly where the main body of flooding is concerned. There are three main areas where waters recede during the 5-day period: to the east of the image on the Wharfe, towards the north of the image below York, and downstream of the confluence of the two rivers. However, as mentioned previously, VV polarisation produces an erroneously reduced flood extent for 1 January, with areas of flooding likely missing from this analysis.

The other main bodies of flooding around the Wharfe and Ouse display minimal change in surface area. However, it can be observed that on the 3 January locations within the wider flood boundary are being classed as land rather than flood, particularly along the river reach. This suggests a reduction in the depth of water, allowing features such as river banks to protrude the water surface.
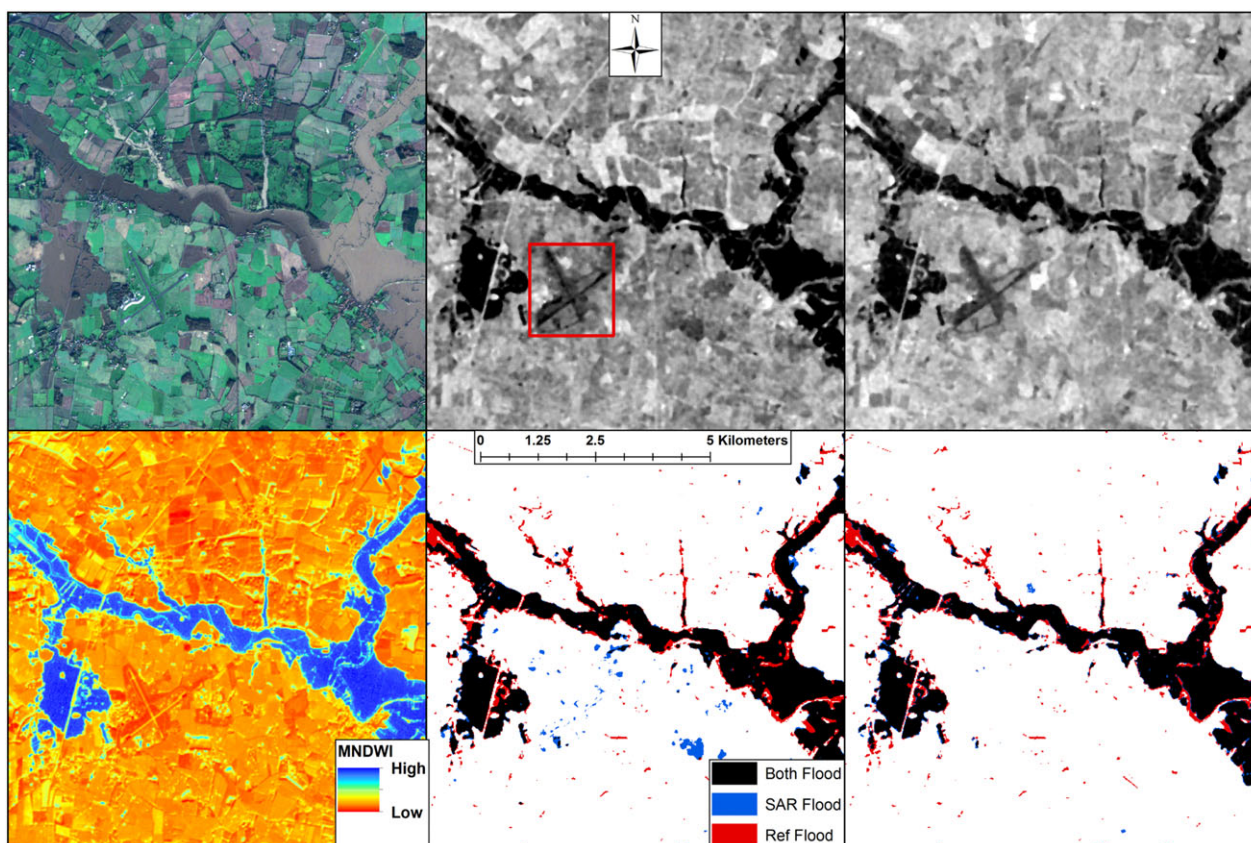
Figure 6 Validation of the results for a subset of the region against the Sentinel-2 image. (Top left) True colour composite Sentinel-2 satellite image for 29 December. (Top middle) Sentinel-1 SAR image for 29 December, VH polarisation. The location of the described airport is shown by the red box. (Top right) VV polarised SAR image. (Bottom left) MNDWI, calculated from the Sentinel-2 image, with blue representing water. (Bottom middle) Comparison of extracted flood extents, with blue representing those from VH SAR, red from optical and black represents areas identified in both. (Bottom right) VV flood extents compared to reference data set.

To provide an overview of the most flood prone areas in the region an estimate has been made for the number of days each pixel was flooded during the 37-day study period (Figure 9). Both polarisations display a similar pattern along the course of the rivers, with greatest inundation located within the floodplains of the Wharfe and Ouse before the confluence. Some of these areas are shown to have flooded for the whole study period. Downstream of the confluence flooding only occurred after the extreme rainfall experienced during storm Eva, when the peak flood extents are found. There are major differences with the mapping of inundated fields, with some areas identified as flooded for most of the study period within the VH map, whilst only being minimally highlighted by VV.

Comparison with EA FMP

It has been reported that some rivers in the UK exceeded their 100-year return period during the winter 2015–2016 floods (NHMP, 2016). Accordingly, the SAR-derived

inundation extents have been compared to the EA FMP 100 year flood zone, as well as the areas designated for storage of flood water and protected by flood defences (Figure 10).

An area of 53.4 km^2 of the 100-year flood area is undefended, and at risk of flooding during such an event. At peak flood 49.2% (VH) and 48.0% (VV) of these regions were inundated, suggesting the flooding was not a 100-year event in this area at the time of the satellite pass (Figure 11). Within the 100-year flood boundary, 10.4 km^2 has been designated as water storage areas. At maximum, 79.3% and 79.1% of these areas were inundated for VH and VV, respectively, with Figure 10 suggesting the area downstream of the confluence was close to capacity. Arguably, the most important information within the EA FMP is the areas protected from the 100-year event by the flood defences. At peak flood a total of 2.3 km^2 became inundated using the VH data, with 2.2 km^2 for VV, under 10% of the protected areas in the region (Figure 12). This is largely to the west of Figure 10. Overall, the time-series for
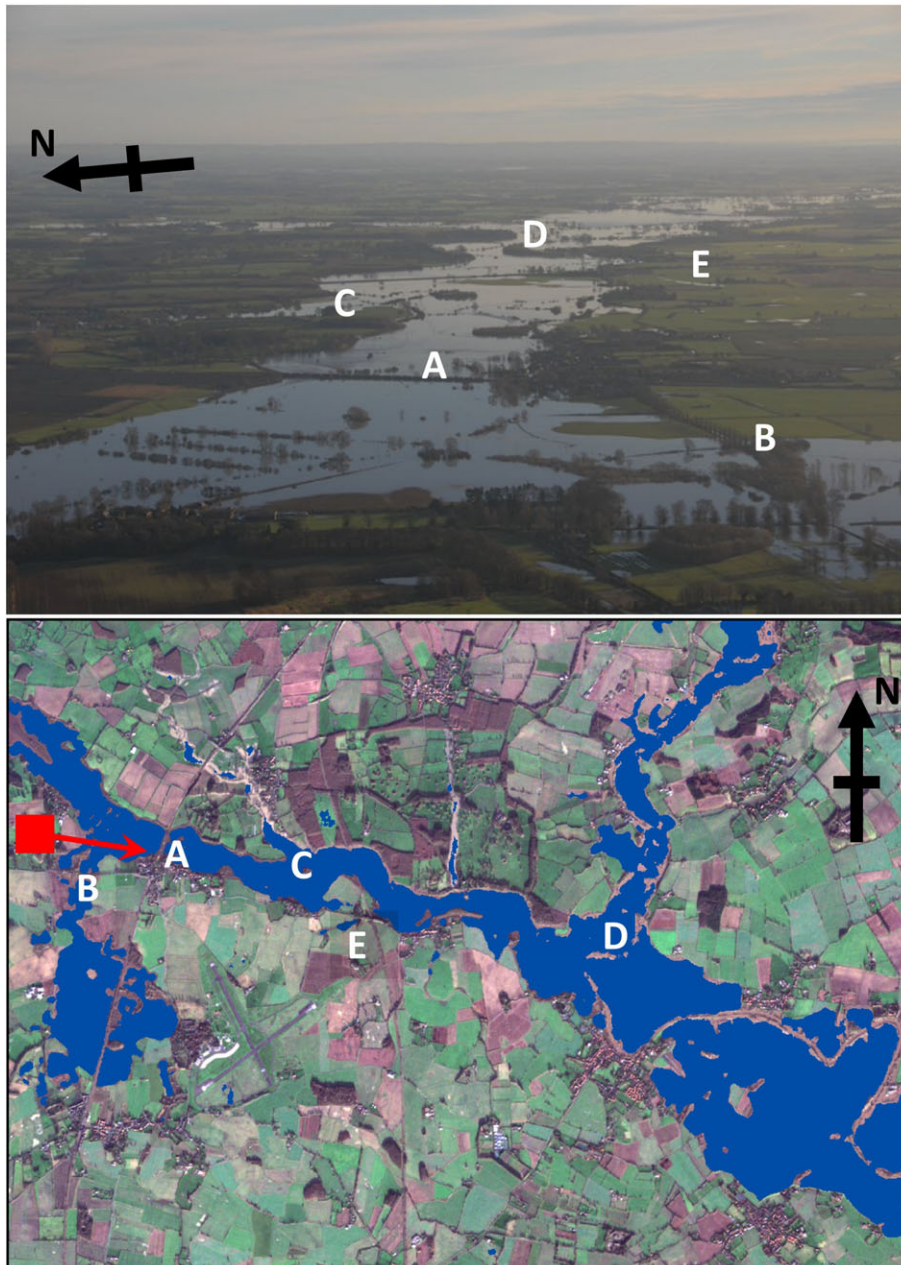
Figure 7 Comparison between an aerial photograph from 27 December (from @NPAS_CarrGate) (top), and the identified flood areas from VV polarised SAR on 29 December (bottom). Red square and arrow show approximate location and viewing direction of the helicopter. Locations A (railway embankment) and B (B1223) provide georeferencing examples. Point C shows The Foss joining the river Wharfe, and point D shows the confluence of the Wharfe and the Ouse. Field level flooding is visible in both data sets, with an example given at E. Differences in flood extent are potentially caused by the 2-day time gap between the images.

flooding for each designated area closely follows the overall flood sequence observed in Figure 3.

The EA FMP largely encompass the main bodies of flooding identified in the satellite data. The percentage of the flooding that occurred outside any of the designated FMP areas has been calculated for each date (Figure 13), with

mean percentages of 18.0% (VH) and 9.5% (VV). There are some dates where identified flood outside of the FMP prediction is high. The 5 December (VH and VV), 20 December (VH), and 22 December (VH) have less than 75% of identified flooding within the FMP areas, with the SAR data all showing a large amount of pluvial flooding on these dates.
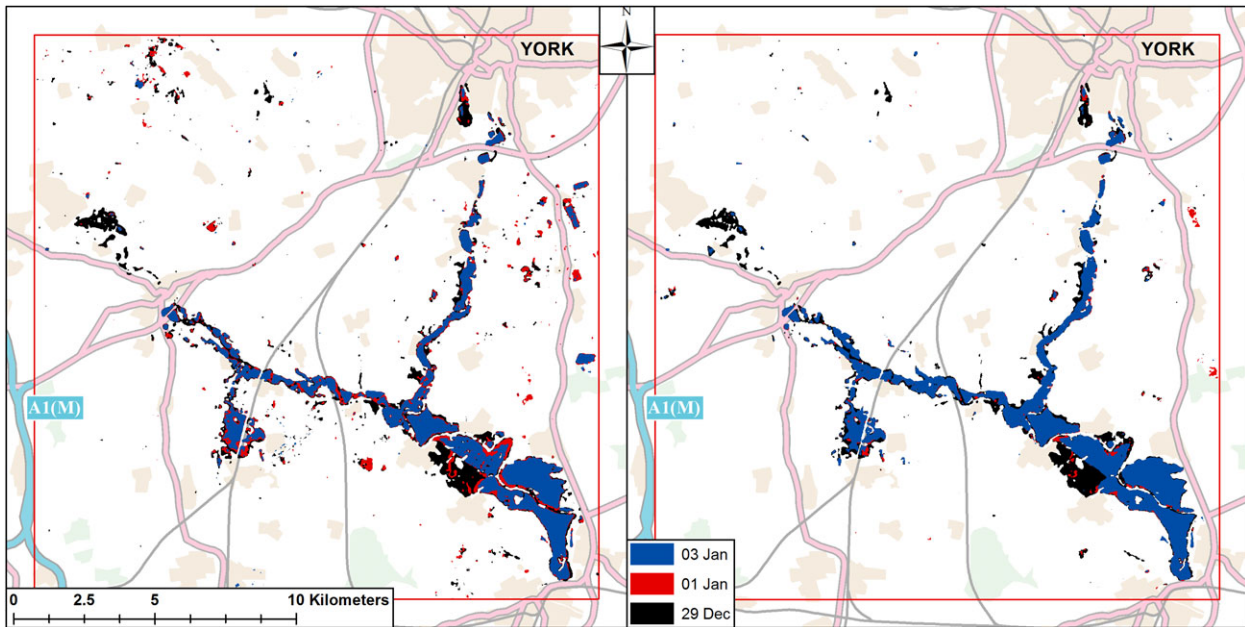
Figure 8 The retreat of flood waters during the aftermath of storm Frank. VH (left) and VV (right) polarisations for satellite orbits on 29 December, 1 January and 3 January are shown.
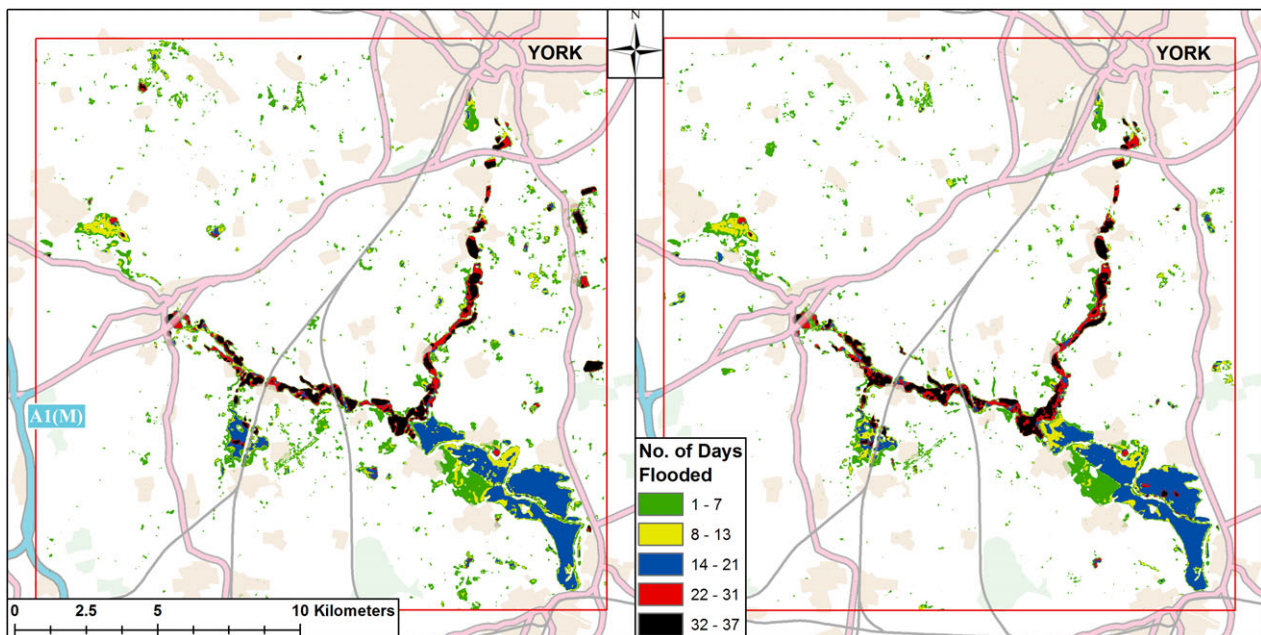

Figure 9 The estimated number of days each pixel is inundated for VH (left) and VV (right) polarisations. Total number of days in the study period is 37. Each image is assigned a number of days representing an even distribution of the time to the preceding and following satellite passes. For each pixel, the images identified as flooded have been summed to provide an estimate total days flooded.

Discussion

The validation of the adapted CDAT results against the Sentinel-2 MNDWI data set provides good correlation for both polarisations. Long *et al.* (2014) completed a similar comparison with optical imagery to determine the total accuracy of the original CDAT method, achieving accuracies ranging between 77.1% and 91.7%. The 97.0% and
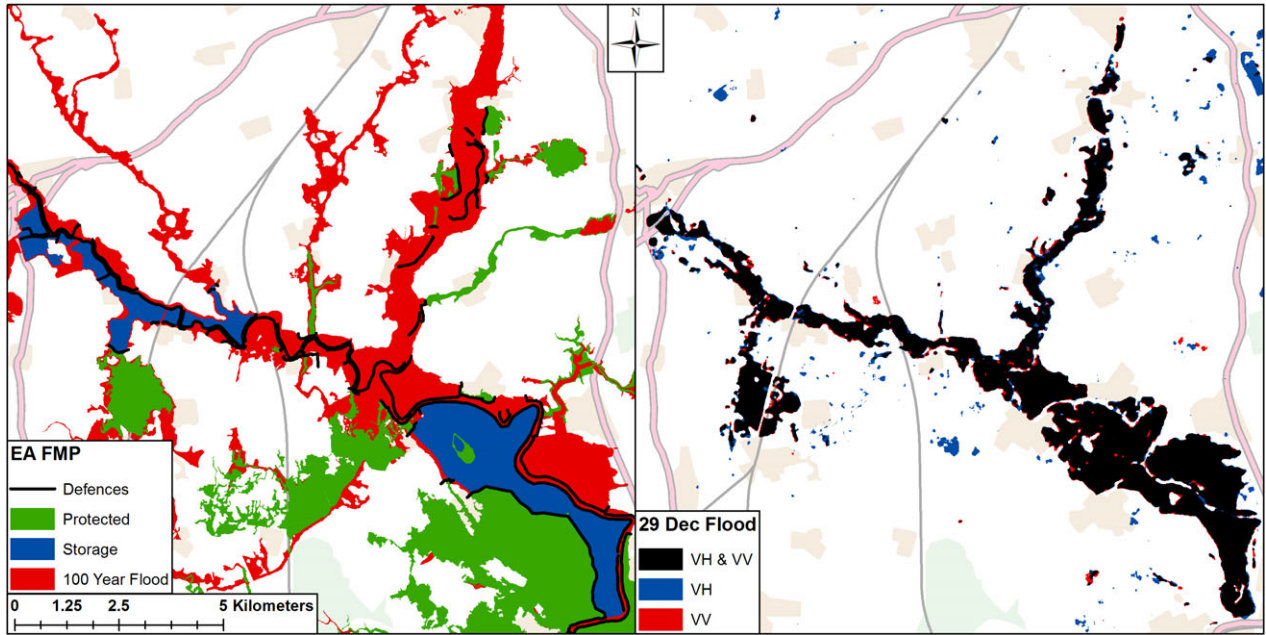
Figure 10 The EA FMP for a subset of the study region (left), showing 1 in 100 year flood, areas protected by flood defences, and flood storage areas outlines. Extracted flood extents for VH, VV and where they overlap for 29 December (right) for comparison.
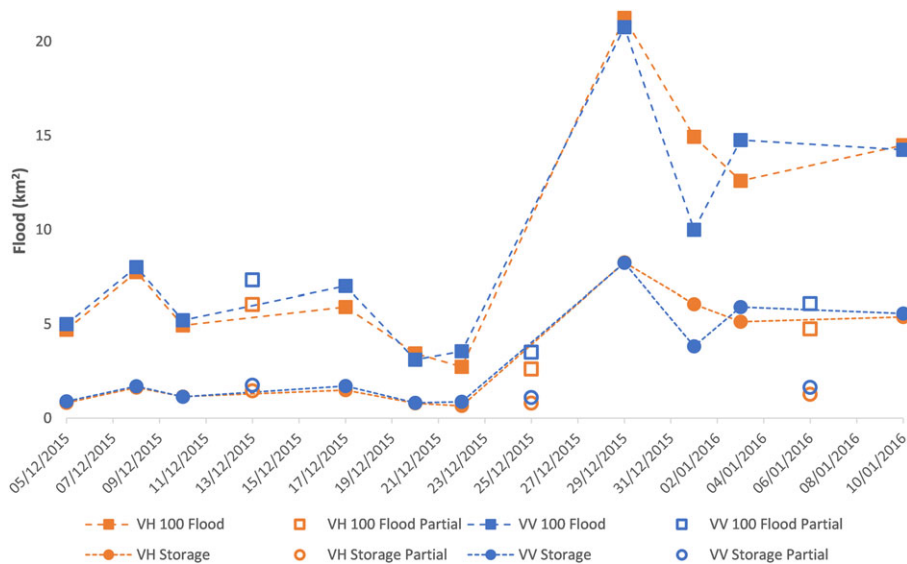

Figure 11 Area of flooding identified within the EA FMP 100 year flood boundary, and the proportion located in a designated flood storage area. Partial data points represent those without full satellite coverage. Total area for the 100-year flood region is 53.4 km^2 (13.4% of the study area), including 10.4 km^2 designated as flood storage areas.

97.4% total accuracies for the VH and VV polarisations achieved in this study suggests the adaption applied to the original method provides an improvement on the original process. Producer's and user's accuracies, and Cohen's kappa coefficient (κ) all provide good results, with sources of misclassification identified in both the SAR and the optical results. Similar to the results presented by Twele *et al.*

(2016), the VV polarisation provided a slight improvement on accuracy compared to VH. However, both polarisations produce similar validation results in this study, and considering the inaccuracies associated with identifying inundation using SAR, it is still unclear which of the two Sentinel-1 polarisations is the preferential choice for delineating flooding.
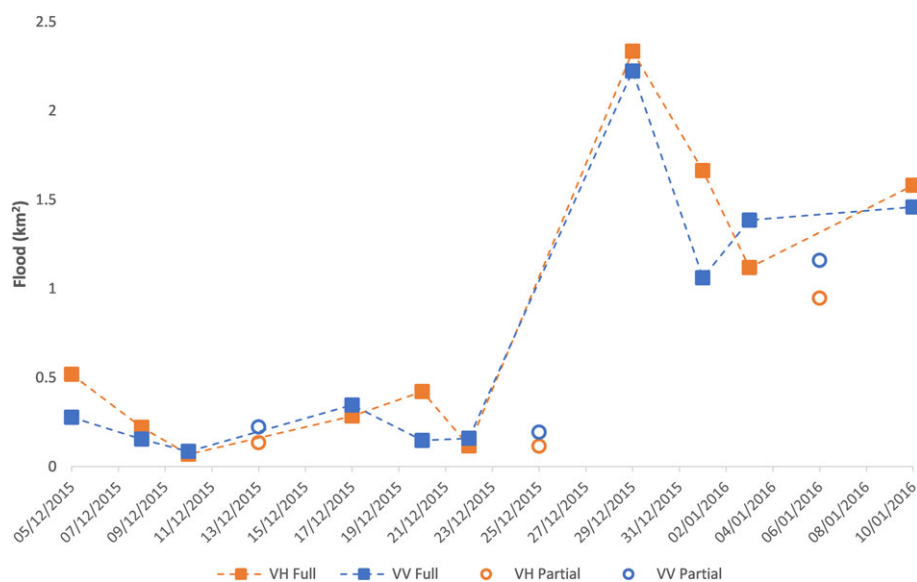
Figure 12 Amount of flooding within the protected areas identified in the EA FMP. Partial data points represent those without full satellite coverage. Protected areas cover 24.9 km^2, or 6.2%, of the study region.
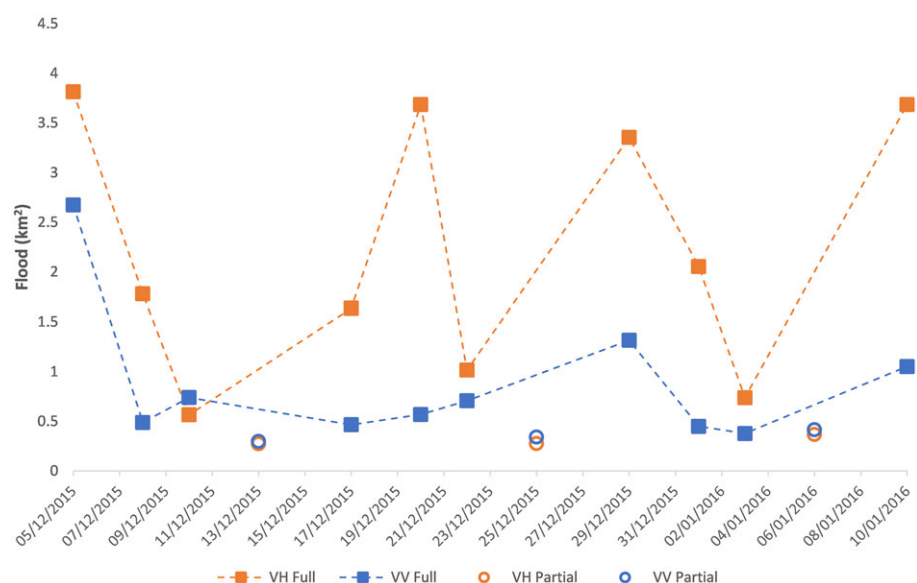

Figure 13 Amount of flooding identified that is not found within the boundaries of the EA FMP. Partial data points represent those without full satellite coverage. 80.4% of the area of interest, or 321.7 km^2, is not included in any of the EA FMP zones.

There are some caveats that require acknowledgement when using optical data to validate the SAR flood extents. It should be noted that optical imagery, as a satellite product, potentially suffers from inaccuracies within the water identification process. Therefore, it cannot be considered as a definitive measure of the accuracy. Furthermore, a single reference image was used in this study, when ideally multiple images would be available to confirm the accuracy of the flood extents from each polarisation. However, the limitations of optical imagery, namely its inability to penetrate cloud cover, restrict the number of available scenes. Within this study the VV flood extents on 1 January appear inadequate when compared to the preceding and following flood extents. This is likely to be caused by the susceptibility of VV to increased backscatter produced by roughening of the water surface due to wind or heavy rain (Brisco et al., 2008; Manjusree et al., 2012). If a suitable optical reference data set was available for this date, it is expected that

the validation outcome would produce a reduced level of accuracy for VV. The variability in perceived results accuracy on non-validation dates highlights the need for further validation of flood extents produced using the two Sentinel-1 polarisations, particularly in varying environmental conditions.

Caution must be exercised in interpreting the data as an accurate representation of the flooding time series due to the sparse nature of the satellite images, with gaps of 2–4 days between the Sentinel-1 scenes. This is exacerbated by satellite crossings not covering the full extent of the study area, potentially underestimating the full extent. As well as the maximum flood extent, the speed of onset and recession is important for stakeholders to fully manage the impacts of an event. The linearity of the rising and falling limbs around the 29 December peak is questionable. Furthermore, the peak extent seen from the images on 29 December is unlikely to capture the true maximum extent. There is no method to accurately extrapolate the data points to determine the timing and magnitude of the peak flood, as well as the onset and recession speed, without the inclusion of *in situ* data. Future events will benefit from the full constellation of two Sentinel-1 satellites, providing a denser time series, allowing a better estimation of the flood dynamics.

One of the advantages of using satellite data to map flood extents is the ability to identify wide-scale pluvial flooding away from the floodplains. This data can be costly and time consuming to collect on the ground, with resources often allocated to urban areas during an event due to the more profound risk and impacts. Flooded fields have been identified using the CDAT methodology, although there is variability between the VH and VV polarisations. Comparing the results to the Sentinel-2 image, it appears likely that VH overestimates field flooding, with VV providing a more plausible representation. Cross-polarised images have been shown to have a wider variance in backscatter from vegetated land covers, potentially creating overlap with the water backscatter ranges, leading to an overestimation of the flood extent (Manjusree *et al.*, 2012; Twele *et al.*, 2016). However, further *in situ* data during times of flood is required to fully understand the relative accuracies of the polarisations, and to help explain the temporal pattern of pluvial flooding.

The EA FMP are used for consultation within the UK building and planning process (Porter and Demeritt, 2012). The clarification of their accuracy provided here supports their continued use for this purpose. Agreement was found between the flood maps and both polarisations of SAR data for the locations of fluvial flooding. Having been created from a hydraulic model, the close correlation between the maps and the satellite data on the floodplains is to be expected. Differences come away from the floodplains, with

the EA FMP not designed to predict the location of pluvial or groundwater flooding.

The newly available free satellite data sets at spatial resolutions suitable for flood mapping can greatly improve the ability of stakeholders to monitor events. Sentinel-1 data is typically available within a few hours of the satellite pass, allowing for near-real time analysis of the flood extent. Furthermore, automation of the above processes is achievable, as the only process that required human interaction was determination of the global SAR threshold used to create the final filtering step. Although the applied threshold can be used for future studies, care is needed as both satellite and ground conditions can change. Scene by scene automated threshold determination will provide the most accurate delineation of water from the SAR flood image.

There are no restrictions on locations with the CDAT methodology presented here. The two satellite constellation of Sentinel-1 provides coverage between 1 and 3 days depending on latitude (ESA, 2016a, 2016b), an improvement on previous SAR satellites. The 5-metre DTM used to create the HAND and slope components of the terrain filter is a UK only data set, however, there are freely available high resolution global topographic data sets that can be used for this purpose with similar results. Further investigations in different geographical settings will confirm the threshold parameters used in this study, providing a tool that can be used to estimate flood extent globally.

Despite the advantages of satellite based flood monitoring, the temporal resolution can still result in flood onset, maximum and recession to be missed (Sanyal and Lu, 2004). When completing regional scale studies using satellite data sources, there is a high probability that each satellite orbit will not cover the full area. An understanding of the limitations of satellite acquisition parameters, including the potential for temporal and spatial data gaps, needs to sufficiently communicated to stakeholders to allow for considerations to be made in any analysis, and to minimise any assumptions based on extrapolated results.

Conclusion

An adapted change detection and thresholding methodology has been developed using 13 Sentinel-1 images to map the flooding experienced in Yorkshire during the 2015–2016 UK winter storm season. The difference between the SAR data and a median reference image has been filtered and thresholded to determine the flood extent. The process adapts the previous CDAT methodology proposed by Long *et al.* (2014), with adjustments to the filtering composition and processes, including the addition of a

new step to remove misclassification due to seasonal changes in land cover.

Peak flood extents occurred on 29 December 2015, during the immediate aftermath of the severe rainfall during storms Eva and Frank. On the same date a Sentinel-2 optical satellite image was collected for the region, allowing direct comparison between the results. MNDWI and Otsu's method was used to determine the optical flood extent. User's and Producer's accuracies of at least 87.0% and 71.5% were found for the two polarisations, with Cohen's κ of 0.778 and 0.799 for VH and VV, respectively. The slightly improved accuracy observed using the VV polarisation matches similar results obtained by Twele *et al.* (2016), although on other dates VV appears to underestimate the water extent, likely caused by wind roughening of the water surface.

The EA FMP provide the outline of a 100-year flood event, as well as areas protected by flood defences and those used to store flood waters. The extracted outlines from the recent winter flooding provide a good comparison data set to the predictive maps. At peak flood approximately 49% of the expected 100-year flood region became inundated, with the incorporated designated flood storage areas at 79% capacity in terms of surface area. Approximately 9% of the protected areas, representing 2.3 km^2, was flooded during this time. The predictive maps provided a good estimate of fluvial flooding, with the extent matched by the SAR data. Differences come with the identification of pluvial flooding, information that is not modelled in the EA FMP. The identification of flooding in these rural areas will be useful in helping to minimise the impacts to local stakeholders.

Improvements can be made with the methodology presented by clarifying the accuracy of flood identification via further validation, particularly for smaller scale pluvial inundation, and with the removal of misclassified urban features. However, the total accuracy of the two polarisations is good, with both above 97%, and the methodology can be used as an easy to implement, autonomous, near-real time flood monitoring tool. Refinement of the methodology is ongoing, and further validation of results against recent UK and global flood events will confirm the potential of SAR data and the methods for use in flood management.

Acknowledgements

References

Alsdorf D.E., Rodriguez E. & Lettenmaier D.P. Measuring surface water from space. *Rev Geophys* 2007, **45**, (2), RG2002. https://doi.org/10.1029/2006RG000197.

Brisco B., Touzi R., van der Sanden J.J., Charbonneau F., Pultz T.J. & D'Iorio M. Water resource applications with RADARSAT-2 – a preview. *Int J Digit Earth* 2008, **1**, (1), 130–147. https://doi.org/10.1080/17538940701782577.

Brivio P.A., Colombo R., Maggi M. & Tomasoni R. Integration of remote sensing data and GIS for accurate mapping of flooded areas. *Int J Remote Sens* 2002, **23**, (3), 429–441. https://doi.org/10.1080/01431160010014729.

Brown K.M., Hambidge C.H. & Brownett J.M. Progress in operational flood mapping using satellite synthetic aperture radar (SAR) and airborne light detection and ranging (LiDAR) data. *Prog Phys Geogr* 2016, **40**, (2), 196–214. https://doi.org/10.1177/0309133316633570.

De Zan F. & Guarnieri A.M. TOPSAR: terrain observation by progressive scans. *IEEE Trans Geosci Remote Sens* 2006, **44**, (9), 2352–2360. https://doi.org/10.1109/TGRS.2006.873853.

Esch T., Schenk A., Ullmann T., Thiel M., Roth A. & Dech S. Characterization of land cover types in TerraSAR-X Images by combined analysis of speckle statistics and intensity information. *IEEE Trans Geosci Remote Sens* 2011, **49**, (6), 1911–1925. https://doi.org/10.1109/TGRS.2010.2091644.

European Space Agency. SENTINEL-1 SAR User Guide. 2016a. Available at: https://sentinel.esa.int/web/sentinel/user-guides/sentinel-1-sar [accessed 30 September 2016].

European Space Agency (ESA). Sentinel-1 SAR: Revisit and Coverage. 2016b. Available at: https://sentinel.esa.int/web/sentinel/user-guides/sentinel-1-sar/revisit-and-coverage [accessed 30 September 2016].

Feyisa G.L., Meilby H., Fensholt R. & Proud S.R. Automated water extraction index: a new technique for surface water mapping using Landsat imagery. *Remote Sens Environ* 2014, **140**, 23–35. https://doi.org/10.1016/j.rse.2013.08.029.

Gan T.Y., Zunic F., Kuo C.-C. & Strobl T. Flood mapping of Danube River at Romania using single and multi-date ERS2-SAR images. *Int J Appl Earth Obs Geoinf* 2012, **18**, 69–81. https://doi.org/10.1016/j.jag.2012.01.012.

Geudtner D., Torres R., Snoij P., Davidson M. & Rommen B. Sentinel-1 systems capabilities and applications. In: *2014 I.E. International Geoscience and Remote Sensing Symposium (IGARSS)*. New York: IEEE, 2014, 1457–1460. https://doi.org/10.1109/IGARSS.2014.6946711.

Giustarini L., Hostache R., Matgen P. & Schumann G.J.P. A change detection approach to flood mapping in urban areas using TerraSAR-X. *IEEE Trans Geosci Remote Sens* 2013, **51**, (4), 2417–2430. https://doi.org/10.1109/TGRS.2012.2210901.

Giustarini L., Vernieuwe H., Verwaeren J., Chini M., Hostache R., Matgen P., Verhoest N.E.C. & De Baets B. Accounting for image uncertainty in SAR-based flood mapping. *Int J Appl Earth Obs Geoinf* 2015, **34**, 70–77. https://doi.org/10.1016/j.jag.2014.06.017.

Google Earth Engine (GEE). Sentinel-1: C-band Synthetic Aperture Radar (SAR) Ground Range Data, log scaling. 2015. Available at: https://explorer.earthengine.google.com/#detail/COPERNICUS%2FS1_GRD [accessed 30 September 2016].

Grimaldi S., Li Y., Pauwels V.R.N. & Walker J.P. Remote sensing-derived water extent and levels to constrain hydraulic flood forecasting models: opportunities and challenges. *Surv Geophys* 2016, **37**, (5), 977–1034. https://doi.org/10.1007/s10712-016-9378-y.

Henry J.B., Chastanet P., Fellah K. & Desnos Y.L. Envisat multi-polarized ASAR data for flood mapping. *Int J Remote Sens* 2006, **27**, (9–10), 1921–1929. https://doi.org/10.1080/01431160500486724.

Horritt M.S., Mason D.C. & Luckman A.J. Flood boundary delineation from synthetic aperture radar imagery using a statistical active contour model. *Int J Remote Sens* 2001, **22**, (13), 2489–2507. https://doi.org/10.1080/01431160116902.

Hostache R., Matgen P. & Wagner W. Change detection approaches for flood extent mapping: How to select the most adequate reference image from online archives? *Int J Appl Earth Obs Geoinf* 2012, **19**, (1), 205–213. https://doi.org/10.1016/j.jag.2012.05.003.

Jung H.C., Hamski J., Durand M., Alsdorf D., Hossain F., Lee H., Hossain A., Hasan K., Khan A.S. & Hoque A. Characterization of complex fluvial systems using remote sensing of spatial and temporal water level variations in the Amazon, Congo, and Brahmaputra Rivers. *Earth Surf Process Landf* 2010, **35**, (3), 294–304. https://doi.org/10.1002/esp.1914.

Long S., Fatoyinbo T.E. & Policelli F. Flood extent mapping for Namibia using change detection and thresholding with SAR. *Environ Res Lett* 2014, **9**, 35002–35009. https://doi.org/10.1088/1748-9326/9/3/035002.

Manjusree R., Kumar L.P., Bhatt C.M., Rao G.S. & Bhanumurthy V. Optimization of threshold ranges for rapid flood inundation mapping by evaluating backscatter profiles of high incidence angle SAR images. *Int J Disaster Risk Sci* 2012, **3**, (2), 113–122. https://doi.org/10.1007/s13753-012-0011-5.

Martinis S., Kersten J. & Twele A. A fully automated TerraSAR-X based flood service. *ISPRS J Photogram Remote Sens* 2015, **104**, 203–212. https://doi.org/10.1016/j.isprsjprs.2014.07.014.

Mason D.C., Davenport I.J., Neal J., Schumann G.J.P. & Bates P.D. Near real-time flood detection in urban and rural areas using high resolution Synthetic Aperture Radar images. *IEEE Trans Geosci Remote Sens* 2012, **50**, (8), 3041–3052. https://doi.org/10.1109/TGRS.2011.2178030.

Matgen P., Hostache R., Schumann G.J.P., Pfister L., Hoffmann L. & Savenije H.H.G. Towards an automated SAR-based flood monitoring system: lessons learned from two case studies. *Phys Chem Earth* 2011, **36**, (7–8), 241–252. https://doi.org/10.1016/j.pce.2010.12.009.

McFeeters S.K. The use of normalised difference water index (NDWI) in the delineation of open water features. *Int J Remote Sens* 1996, **17**, 1425–1432.

National Hydrological Monitoring Programme (NHMP). Hydrological Summary for the United Kingdom – Dec 2015. 2016. Available at: http://nora.nerc.ac.uk/512654/ [accessed 29 September 2016].

Nobre A.D., Cuartas L.A., Hodnett M., Renno C.D., Rodrigues G., Silveira A., Waterloo M. & Saleska S. Height above the nearest drainage – a hydrologically relevant new terrain model. *J Hydrol* 2011, **404**, (1–2), 13–29. https://doi.org/10.1016/j.jhydrol.2011.03.051.

Otsu N. Threshold selection method from gray-level histograms. *IEEE Trans Syst Man Cybern* 1979, **9**, (1), 62–66.

Porter J. & Demeritt D. Flood-risk management, mapping, and planning: the institutional politics of decision support in England. *Environ Plan A* 2012, **44**, (10), 2359–2378. https://doi.org/10.1068/a44660.

Pradhan B., Hagemann U., Tehrany M.S. & Prechtel N. An easy to use ArcMap based texture analysis program for extraction of flooded areas from TerraSAR-X satellite image. *Comput Geosci* 2014, **63**, 34–43. https://doi.org/10.1016/j.cageo.2013.10.011.

Pulvirenti L., Chini M., Pierdicca N. & Boni G. Use of SAR for detecting floodwater in urban and agricultural areas: the role of the interferometric coherence. *IEEE Trans Geosci Remote Sens* 2016, **54**, (3), 1532–1544. https://doi.org/10.1109/TGRS.2015.2482001.

Rees W.G. Simple masks for shadowing and highlighting in SAR images. *Int J Remote Sens* 2000, **21**, (11), 2145–2152. https://doi.org/10.1080/01431160050029477.

Rennó C.D., Nobre A.D., Cuartas L.A., Soares J.V., Hodnett M.G., Tomasella J. & Waterloo M.J. HAND, a new terrain descriptor using SRTM-DEM: Mapping terra-firme rainforest environments in Amazonia. *Remote Sens Environ* 2008, **112**, (9), 3469–3481. https://doi.org/10.1016/j.rse.2008.03.018.

Sanyal J. & Lu X.X. Application of remote sensing in flood management with special reference to monsoon Asia: a review. *Nat Hazards* 2004, **33**, (2), 283–301. https://doi.org/10.1023/B:NHAZ.0000037035.65105.95.

Schlaffer S., Matgen P., Hollaus M. & Wagner W. Flood detection from multi-temporal SAR data using harmonic analysis and change detection. *Int J Appl Earth Obs Geoinf* 2015, **38**, 15–24. https://doi.org/10.1016/j.jag.2014.12.001.

Schumann G.J.P., Bates P.D., Horritt M.S., Matgen P. & Pappenberger F. Progress in integration of remote sensing-

© 2017 The Authors.

Journal of Flood Risk Management published by Chartered Institution of Water and Environmental Management and John Wiley & Sons Ltd.

J Flood Risk Management (2017)

derived flood extent and stage data and hydraulic models. *Rev Geophys* 2009, 47, RG4001. https://doi.org/10.1029/2008RG000274.

Twele A., Cao W.X., Plank S. & Martinis S. Sentinel-1-based flood mapping: a fully automated processing chain. *Int J Remote Sens* 2016, **37**, (13), 2990–3004. https://doi.org/10.1080/01431161.2016.1192304.

Xu H.Q. Modification of normalised difference water index (NDWI) to enhance open water features in remotely sensed imagery. *Int J Remote Sens* 2006, **27**, (14), 3025–3033.